

## Article

# Novel Terahertz Properties of Nanostructured $Mn_{3+0.53}Sn$ Films with Different Crystalline Orientations Driven by Ostwald Ripening on (0001) $c-Al_2O_3$

Shaopeng Yang <sup>1,†</sup>, Xinyue Wang <sup>1,†</sup>, Qiujin Wang <sup>2,†</sup>, Tong Xu <sup>1</sup>, Qian Wang <sup>1</sup>, Jin Guo <sup>1</sup>, Jian Zuo <sup>1</sup>, Cunlin Zhang <sup>1</sup>, Wen Xu <sup>2,\*</sup>, Yujun Song <sup>3,\*</sup>, Ying Liu <sup>4</sup>, Jing Wang <sup>5</sup> and Hai Wang <sup>1,\*</sup>

<sup>1</sup> Department of Physics, Capital Normal University, Beijing 100048, China

<sup>2</sup> School of Physics and Astronomy, Yunnan University, Kunming 650091, China

<sup>3</sup> Center for Modern Physics Technology, School of Mathematics and Physics, University of Science and Technology Beijing, Beijing 100083, China

<sup>4</sup> College of Chemistry, Beijing Normal University, Beijing 100875, China

<sup>5</sup> School of Physical Sciences, University of Chinese Academy of Sciences, Beijing 100190, China

\* Correspondence: wenxu\_issp@aliyun.com (W.X.); songyj@ustb.edu.cn (Y.S.); wanghai@cnu.edu.cn (H.W.)

† These authors contributed equally to this work.

**Abstract:** The characteristic energies of elementary excitations and collective modes in many quantum materials lie mostly in the terahertz (THz) frequency range, which provides a wide space for the development of THz optical materials and devices. In particular, topological Weyl semimetal  $Mn_3Sn$  is a noncollinear antiferromagnet with anomalous THz properties, which is strongly affected by thermal energy and external magnetic fields. Despite the explosive growth of the research on magnetic Weyl semimetals recently, its nanoscale structure for applications in THz optical devices remains to be explored. Here, we fabricated nanostructured  $Mn_{3+0.53}Sn$  films with different crystal orientations, driven by Ostwald Ripening (OR) on (0001)  $c-Al_2O_3$ . A huge anisotropic THz response manifested a firm link between the optical properties of Weyl antiferromagnet  $Mn_3Sn$  and its contrivable spin structures. The topological properties of  $Mn_3Sn$  are robustly protected in its nanostructures. This work can provide a new horizon for the fabrication of a nanostructured magnetic Weyl alloy and for its potential applications in subwavelength high-performance THz devices.

**Keywords:** nanostructured film;  $Mn_3Sn$ ; Weyl semimetal; terahertz property; Ostwald Ripening



**Citation:** Yang, S.; Wang, X.; Wang, Q.; Xu, T.; Wang, Q.; Guo, J.; Zuo, J.; Zhang, C.; Xu, W.; Song, Y.; et al. Novel Terahertz Properties of Nanostructured  $Mn_{3+0.53}Sn$  Films with Different Crystalline Orientations Driven by Ostwald Ripening on (0001)  $c-Al_2O_3$ . *Coatings* **2022**, *12*, 1201. <https://doi.org/10.3390/coatings12081201>

Academic Editor: Francesco Di Quarto

Received: 28 June 2022

Accepted: 7 August 2022

Published: 17 August 2022

**Publisher's Note:** MDPI stays neutral with regard to jurisdictional claims in published maps and institutional affiliations.



**Copyright:** © 2022 by the authors. Licensee MDPI, Basel, Switzerland. This article is an open access article distributed under the terms and conditions of the Creative Commons Attribution (CC BY) license (<https://creativecommons.org/licenses/by/4.0/>).

## 1. Introduction

The emergence of topological properties with quantum phases in an electronic material can provide an entirely new opportunity for the development of novel optoelectronic materials and devices. Particularly, Weyl semimetals (WSM) can break either the time-reversal or the inversion symmetry. Strongly correlated Weyl semimetals such as  $Mn_3Sn$  are topological materials incorporated with an exquisite magnetism [1–18]. It theoretically suggests that a broadband absorption can be observed for  $Mn_3Sn$  in terahertz (THz) to the midinfrared range [1]. Experimentally, either large anomalous Hall conductivity at room temperature [2] or resonance-enhanced Faraday rotation at low temperature [3] has indisputably demonstrated the fascinating features of  $Mn_3Sn$  in the THz domain.

$Mn_3Sn$  is a hexagonal antiferromagnet with the ABAB stacking sequence of the kagome plane with the inverse triangular spin configuration of Mn (Figure 1a), which engenders a strong anomalous Hall response [4]. It has been shown that this response is linked to the magnetic order and can be manipulated through it [5]. The small net ferromagnetic moment of magnetic octupoles is essential for the external magnetic field to control the spin structure of  $Mn_3Sn$  on the kagome plane and hence the associated electronic states around the Weyl nodes [6–8]. In  $Mn_3Sn$ , the density of states can be extremely low and even vanishes at the Weyl points, which results in a very low charge-carrier density. The

Berry phase and the Berry curvature, that is, the magnetic flux and field in the momentum space, respectively, strongly govern the high anisotropic anomalous transport and optical properties  $\text{Mn}_3\text{Sn}$  [4,7]. It is also known that the topological property of  $\text{Mn}_3\text{Sn}$  is protected, and its responses are robust against composition variations, impurities, lattice imperfections and thermal fluctuation [19].  $\text{Mn}_3\text{Sn}$  based nanodevices with a given crystal orientation and a specific nanostructure thus urgently need to be explored and examined from a viewpoint of the application.

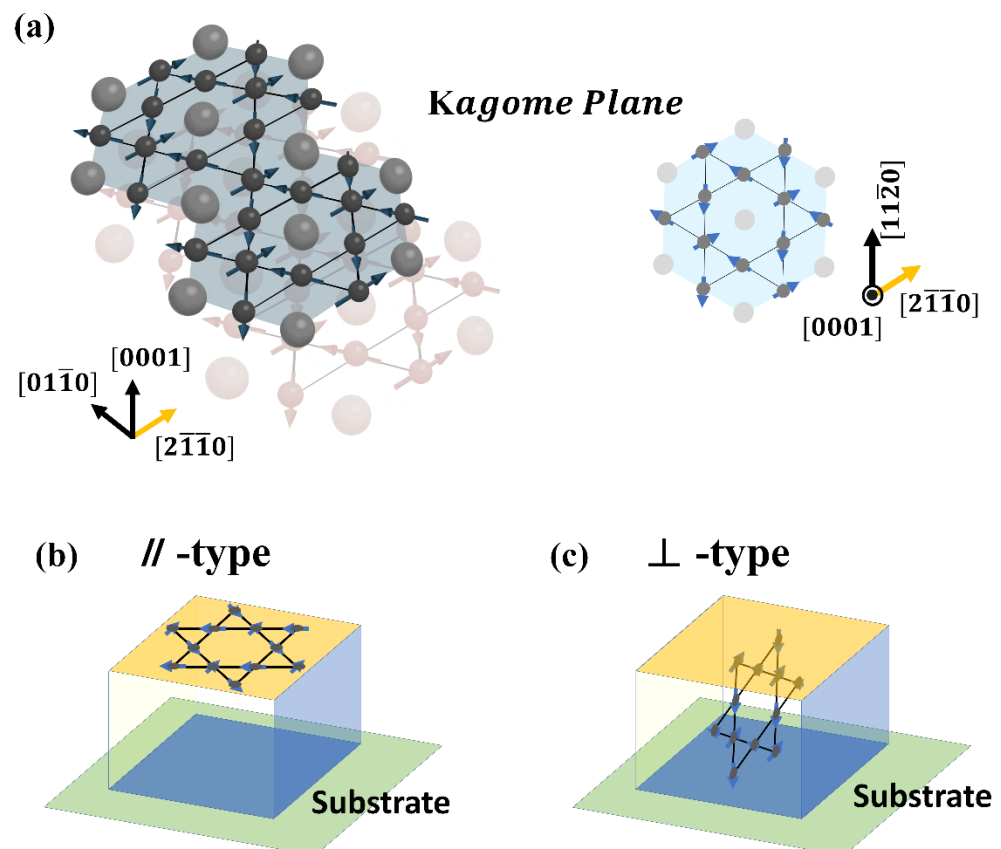


**Figure 1.** A schematic plot of crystal and spin structure of  $\text{Mn}_3\text{Sn}$ . (a) A 3D schematic view of atomic configuration and magnetic texture in the kagome lattice. Coordinates  $(0001)$ ,  $(01\bar{1}0)$  and  $(2\bar{1}\bar{1}0)$  are displayed on the left plot and  $(0001)$ ,  $(11\bar{2}0)$  and  $(2\bar{1}\bar{1}0)$  are illustrated on the right one. A three-sublattice noncollinear antiferromagnetic ordering of Mn, driven by geometrical frustration, presents a weak magnetization along the  $(2\bar{1}\bar{1}0)$  below the Néel temperature ( $T_N \approx 420$  K). This spin texture is viewed as ferroic ordering of cluster magnetic octupoles.  $\text{Mn}_3\text{Sn}$  films with crystalline orientation are demonstrated in (b,c), representing the kagome plane in the plane of the film ( $//$ -type) and the kagome plane perpendicular to the plane of the film ( $\perp$ -type), respectively.

To exploit the unique properties of  $\text{Mn}_3\text{Sn}$  for spintronic/optoelectronic devices, it is significant and important to fabricate the nanostructured  $\text{Mn}_3\text{Sn}$  films with two distinct orientations,  $//$ -type and  $\perp$ -type, as shown in Figure 1b,c. These two types of  $\text{Mn}_3\text{Sn}$  samples have been the focus in recent years. By selecting the facets of a single-crystal oxide substrate (such as  $\text{MgO}$  or  $\text{Al}_2\text{O}_3$ ), either the  $(0001)$  or  $(11\bar{2}0)$  plane epitaxial growth of  $\text{Mn}_3\text{Sn}$  films at elevated temperatures has been revealed [3,9,10]. Although the majority of the work on  $\text{Mn}_3\text{Sn}$  to date has focused on its single crystal [4,6,7,13,14], polycrystalline  $\text{Mn}_3\text{Sn}$  film is a subject in current experimental studies, although it has a certain atomic disorder [17]. In the present work, nanostructured  $\text{Mn}_{3+0.53}\text{Sn}$  films with different crystalline orientations were firstly fabricated on  $(0001)$   $c\text{-Al}_2\text{O}_3$  substrate without metallic seed/buffer layers. A large anisotropic THz transmittance in the samples with different spin textures was

demonstrated experimentally in a wide temperature range, which is consistent with the unique kagome physics of  $\text{Mn}_3\text{Sn}$  and implies the promising potential for its application in THz materials and devices.

## 2. Experiment

Nanostructured  $\text{Mn}_{3+0.53}\text{Sn}$  films (40–330 nm) were fabricated on single-crystal (0001)  $c\text{-Al}_2\text{O}_3$  by molecular beam epitaxy, under an ultrahigh vacuum in a confocal configuration. The base vacuum reached  $1 \times 10^{-7}$  Pa and the deposition pressure was maintained at  $\leq 10^{-6}$  Pa. The deposition rate of Mn and Sn were well controlled at 0.1 Å/s and 0.165 Å/s, respectively, for all samples. The nominal atomic ratio of Mn and Sn was 3.53:1. The  $\text{Mn}_3\text{Sn}$  layers with different thicknesses were deposited at a substrate temperature in the range of room temperature (RT) to 420 °C, and the in situ post annealing was performed at 100–450 °C for 1–10 h, according to the predetermined objectives. The crystallography of the films was examined using a Bruker D8 X-ray diffractometer (XRD, Bruker, Billerica, MA, USA). The surface nanomorphology and cross-section images of the samples were acquired by a Hitachi S-4800 scanning electron microscope (SEM, Hitachi, Tokyo, Japan). A hexagonal  $D0_{19}$   $\text{Mn}_3\text{Sn}$  phase was confirmed by the XRD and selected area electron diffraction using a high-resolution transmission electron microscope (HRTEM-SAED, TiTan ETEM, Thermofisher Scientific, Waltham, MA, USA) in the  $\text{Mn}_{3+0.53}\text{Sn}$  thin films. The large-scale surface morphology was scanned by a Multimode-8 atomic force microscope (AFM, Bruker, Billerica, MA, USA).

Home-built THz time-domain spectroscopy (THz-TDS) was used for the terahertz measurements in a transmission setup over a range of temperatures. The THz pulse is generated by a ZnTe photoconductive antenna and detected by a ZnTe crystal via electro-optic sampling. During the measurements, a magnetic field provided by a closed-cycle 7 T superconducting magnet is applied along the direction perpendicular to the membrane surface. The temperature-dependent THz transmission through the  $\text{Mn}_3\text{Sn}$  sample was measured via increasing temperature from 1.5 K. The effect of the magnetic field was examined after a field cooling down to 1.5 K. All measurements were performed obeying a low-to-high temperature sequence. To avoid THz absorption by air moisture and dust during testing, the main part of the THz system was housed in the dried nitrogen-filled box.

## 3. Results and Discussions

We first present in Figure 2, (0001) and  $(11\bar{2}0)$   $\text{Mn}_{3+0.53}\text{Sn}$  films (240 nm thick) on the (0001)  $c\text{-Al}_2\text{O}_3$  substrate without the metal seed layer. The preparation parameters for all the samples are summarized in Table S1 of a Supplementary File. A strong (0002)  $\text{Mn}_3\text{Sn}$  peak accompanied by a (0004) peak are observed in the XRD for S1, without any noticeable impurity peaks (Figure 2a). The insert in Figure 2a shows the corresponding electron diffraction (SAED) pattern in the selected area of S1 and the  $c\text{-Al}_2\text{O}_3$  substrate. This SAED pattern confirms that S1 is crystallized, and the individual crystal grains possess a hexagonal  $D0_{19}$ -type structure, supporting the interpretation of the epitaxial growth mode since there is a small lattice mismatch ( $\sim 1.7\%$ ) between (0001)  $c\text{-Al}_2\text{O}_3$  and (0001)  $\text{Mn}_3\text{Sn}$ . Nevertheless, the Debye–Scherrer ring in the electron diffraction patterns clearly reveals the polycrystalline nature of S1. Polycrystalline S1 has a complex surface state (Figure 2b), that is, there is a regular geometric structure in each local region, but they fuse with each other forming a wormlike morphology.

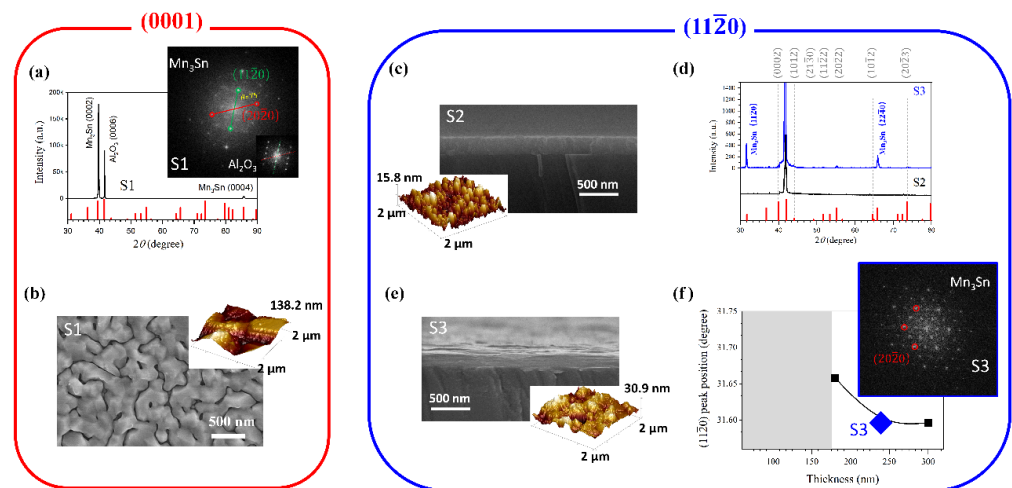


**Figure 2.** Structural characterization and THz measurements of 240 nm thick  $\text{Mn}_{3+0.53}\text{Sn}$  films. The red box emphasizes (0001) sample, while the blue box highlights (11 $\bar{2}$ 0) sample. (a) The XRD profile of the sample grown at 420 °C (S1) and the data of PDF@21-0558 (red lines). The average grain size and the lattice parameters of S1 are  $\sim 100$  nm and  $\sim 4.54\text{\AA}$ , evaluated from its (0002) diffraction peak. Inset: HRTEM-SEDA images of S1 and  $\text{Al}_2\text{O}_3$  substrate. (b) SEM image of S1. Inset:  $2\ \mu\text{m} \times 2\ \mu\text{m}$  AFM image. The root mean square (RMS) roughness is 29.6 nm. (c) Cross-section SEM and AFM images of S2. RMS roughness of S2 is 4.28 nm. (d) XRD patterns of the samples grown at 100 °C, where the black line represents the prepared sample (S2), and the blue curve corresponds to the sample with an in situ post annealing at 450 °C for 5 h (S3). The average grain size and the lattice parameters of S3 are estimated as  $\sim 50$  nm and  $\sim 2.83\text{\AA}$ . (e) Cross-section SEM and AFM images of S3. RMS roughness is 4.28 nm. (f) The (11 $\bar{2}$ 0) diffraction peak position of  $\text{Mn}_{3+0.53}\text{Sn}$  films with different thicknesses. Inset: the HRTEM-SEDA image of S3.

Binary alloy  $\text{Mn}_3\text{Sn}$  has weak binding energy [20]. The melting points of Mn and Sn are 1244 °C and 232 °C, respectively, while the phase formation temperature of the  $\text{Mn}_3\text{Sn}$  films is  $\sim 300\text{--}500$  °C [3,8,21]. Different from Stranski-Krastanow (SK) mode [22], atoms flow from steps with high curvature to steps with low curvature during the film growth driven by OR: small islands shrink, while large islands grow at their expense [23–28]. The migration of the Mn and Sn component is different during the growth at 420 °C. This prevents the uniform thin film deposition although the epitaxial growth criterion is satisfied, which may provide an alternative way for controlling the growth of nano  $\text{Mn}_3\text{Sn}$  films with new and tunable topological properties. More details are provided in Figures S1 and S2 in the supplementary file. In that case, the migration of atoms can be effectively suppressed at a lower deposition temperature. A 240 nm thick  $\text{Mn}_{3+0.53}\text{Sn}$  film grown at 100 °C on a (0001)  $c\text{-Al}_2\text{O}_3$  substrate sample possesses a continuous morphology, which is named as S2 in Figure 2c. However, there is no XRD diffraction peak belonging to a  $\text{Mn}_3\text{Sn}$  phase except for a  $\text{Al}_2\text{O}_3$  (0006) diffraction peak and some weak unknown peaks in S2 (Figure 2d). On the basis of S2, S3 is acquired by an in situ post annealing (PA) with a continuous morphology. As shown in Figure 2d (a solid blue line), there are two obvious peaks at 31.59° and 65.94° in the XRD pattern of S3, which correspond to (11 $\bar{2}$ 0) and (2240) in PDF@21-0558, respectively. Although the cross-section SAED pattern identifies the crystallization with a hexagonal structure, the appearance of (20 $\bar{2}$ 0) structure in the SAED reveals the polycrystalline nature of S3. It is noted that in such a polycrystalline case, a sample with a (11 $\bar{2}$ 0) orientation can only be acquired while its thickness is larger than 180 nm, as illustrated in Figure 2f, which also indicates a non-negligible role of OR in the film growth.

Approaching a thin film limitation, a two-dimensional island feature emerges as displayed in Figure 3a. The nanostructured  $\text{Mn}_{3+0.53}\text{Sn}$  film (40 nm thickness, S4) was deposited at 420 °C on a  $c\text{-Al}_2\text{O}_3$  substrate (more information is provided in Figure S2 in the supplementary file). The multiple peaks in the XRD pattern indicate that S4 belongs

to a  $\perp$ -type film (Figure 3b), with the average grain size of  $\sim 20$  nm and lattice parameters of  $\sim 2.83\text{\AA}$ , rather than a  $\parallel$ -type sample as discussed in S1 (Figure 2a). A post annealing at  $450\text{ }^\circ\text{C}$  for 10 h prompts OR of the  $\text{Mn}_3\text{Sn}$  islands. As shown in Figure 3c, islands with lateral dimensions over 500 nm appear and the spacing between them increases. The grain size of  $\text{Mn}_{3.53}\text{Sn}$  expands to  $\sim 40$  nm, which is twice as large as that of S4. The lattice parameters are  $\sim 4.30\text{\AA}$ . The microstrain  $\varepsilon$  of S4 and S5 are  $\sim 1.71 \times 10^{-3}$  and  $3.5 \times 10^{-4}$ , respectively, which suggests that S4 suffers a higher strain than S5. It is speculated that the density of lattice dislocation in S4 may be much larger than that of S5 [29]. Significantly, as displayed in Figure 3d, the disappearance of the  $(11\bar{2}0)$  peak as well as the strong intensity of the  $(0002)$  peak in the XRD profile of the sample suggest that a  $(0001)$  orienting nanostructured  $\text{Mn}_3\text{Sn}$  film is formed, which is named as S5, belonging to a  $\parallel$ -type sample.

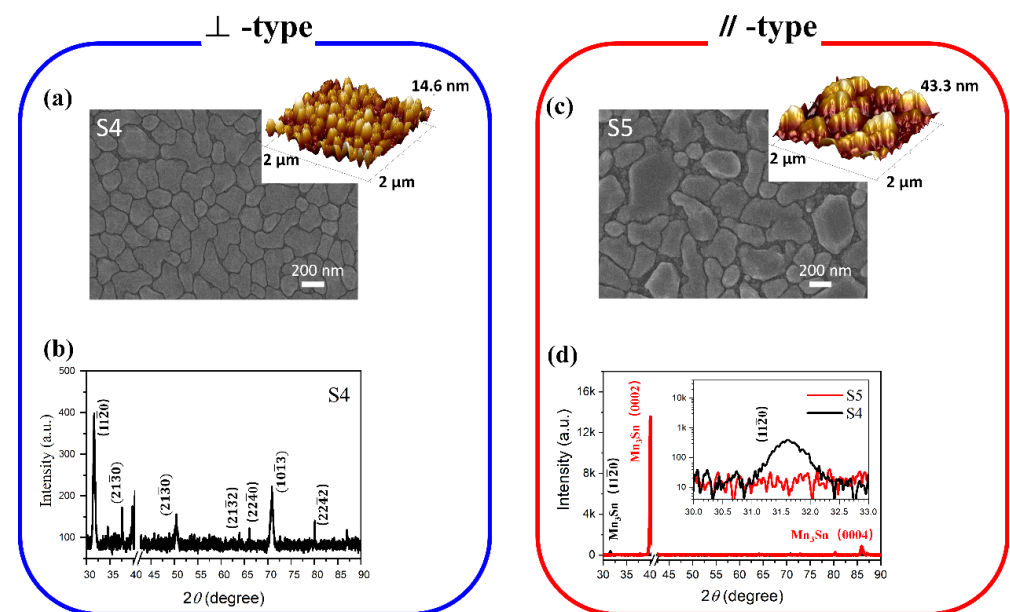


**Figure 3.** Structural characterization of 40 nm  $\text{Mn}_{3+0.53}\text{Sn}$  films. In the blue box: (a) SEM image and (b) XRD data of S4. Inset of (a):  $2\ \mu\text{m} \times 2\ \mu\text{m}$  AFM image. The RMS roughness and the maximum height difference of S4 are 4.12 nm and 14.6 nm, respectively. In the red box: (c) SEM images of S5 (inset: surface AFM images,  $2\ \mu\text{m} \times 2\ \mu\text{m}$ ). (d) XRD patterns of S4 and S5 in the  $30\text{--}90^\circ$  range. Inset: XRD at  $30\text{--}33^\circ$  with a logarithmic ordinate. The RMS roughness is 13.2 nm, and the maximum height difference is 43.4 nm.

In this study, we applied the standard THz-TDS technique to examine the basic optoelectronic properties of  $\text{Mn}_{3+0.53}\text{Sn}$  thin films. The THz transmittance of both S4 and S5 are larger than 0.6, while that of S1 or S3 is much lower than 0.1. Both the main echo peaks and the first echo peaks are detected in all measurements (Figure 4a,b). In the case of  $\parallel$ -type film, S4 (Figure 4a), the time delay between the signals measured at low and high temperatures is small. In contrast, the time delay difference is noticeable in the case of  $\perp$ -type sample, S5 (Figure 4b). The relationships of different quantities in the Faraday geometry are also illustrated schematically by the inserts in Figure 4a,b. The spectra of the real parts of THz optical and magneto-optical conductivities,  $\text{Re}\sigma(\omega)$ , under thin film approximation, are shown at 1.5 K in Figure 4c and at 300 K in Figure 4d, where the results measured at  $H = 0$  and  $H = 7$  T are presented. The following features can be noticed in these spectra. (i) For both  $\parallel$ - and  $\perp$ -type samples,  $\text{Re}\sigma(\omega)$  does not decrease monotonously with increasing  $\omega$  at  $H = 0$  and 7 T, and at 1.5 K and 300 K. This effect indicates that the conducting carriers in  $\text{Mn}_3\text{Sn}$  thin films do not respond to the THz radiation in a conventional way of Drude-like optical conductivity. (ii) Temperature has a relatively weak influence on  $\text{Re}\sigma(\omega)$  for both  $\parallel$ - and  $\perp$ -type samples. (iii) The presence of the external magnetic field  $H$  can affect  $\text{Re}\sigma(\omega)$  for  $\perp$ -type samples, whereas relatively,  $\text{Re}\sigma(\omega)$  for

//-type samples depends on  $H$  indistinctly. (iv) More interestingly,  $\text{Re}\sigma(\omega)$  for //- and  $\perp$ -type samples shows a clear feature of anisotropy, not only for frequency dependence but also for the strength of the optical absorption (noting that  $\text{Re}\sigma(\omega)$  is proportional to the optical absorption coefficient). At  $H = 0$  and  $T = 1.5$  K,  $\text{Re}\sigma(\omega)$  for //- and  $\perp$ -type samples at 0.80 THz are  $5.36 \times 10^3 \Omega^{-1}\cdot\text{cm}^{-1}$  and  $0.28 \times 10^3 \Omega^{-1}\cdot\text{cm}^{-1}$ , respectively. Two curves for  $\text{Re}\sigma(\omega)$  intersect at  $1.1 \times 10^3 \Omega^{-1}\cdot\text{cm}^{-1}$ @1.80 THz (labelled as A). At  $H = 0$  and  $T = 300$  K, the two curves for  $\text{Re}\sigma(\omega)$  intersect at  $0.8 \times 10^3 \Omega^{-1}\cdot\text{cm}^{-1}$ @2.02 THz (Point A); namely blue shifting can be observed in comparison with the case of  $T = 1.5$  K. (v) The presence of a magnetic field can reduce the difference of  $\text{Re}\sigma(\omega)$  for //- and  $\perp$ -type samples in the low THz regime. At  $H = 7$  T and  $T = 1.5$  K, the two curves of  $\text{Re}\sigma(\omega)$  for //- and  $\perp$ -type samples meet at  $1.4 \times 10^3 \Omega^{-1}\cdot\text{cm}^{-1}$ @1.71 THz (labelled as B). At  $H = 7$  T and  $T = 300$  K,  $\text{Re}\sigma(\omega)$  for  $\perp$ -type samples reaches  $3.34 \times 10^3 \Omega^{-1}\cdot\text{cm}^{-1}$  at 0.80 THz. The point B locates at  $1.34 \times 10^3 \Omega^{-1}\cdot\text{cm}^{-1}$ @1.74 THz without an obvious shift in comparison with that measured at  $T = 1.5$  K in Figure 4c. The results shown in Figure 4c and 4d imply that a huge anisotropic THz response can remain in a wide temperature range.

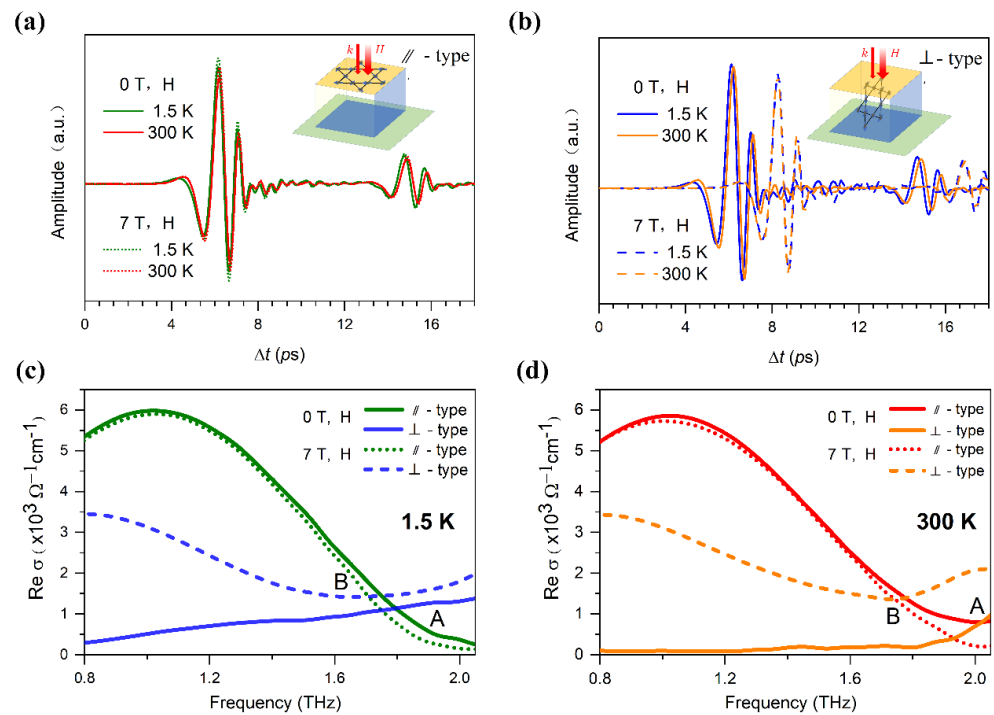


**Figure 4.** THz measurements of 40 nm  $\text{Mn}_{3+0.53}\text{Sn}$  samples. (a,b) are the THz-TDS of //- and  $\perp$ -type samples (S5 and S4), respectively, where the abscissa  $\Delta t$  is the time difference between signals of sample and the system. Inset plots are schematical illustrations for the geometric relationship in measurement between the kagome plane, the film surface, the wave vector ( $k$ ) of incident terahertz wave and the external magnetic field ( $H$ ). The real parts of the conductivities of //- and  $\perp$ -type samples are displayed in (c) at 1.5 K and in (d) at 300 K.

Now, we examine the temperature- and magnetic-field-dependent optical coefficients obtained from the THz-TDS measurements for the 40 nm thick  $\text{Mn}_{3+0.53}\text{Sn}$  films. The temperature dependence of the intersection points A and B are shown in Figure 5a. As mentioned above (see Figure 4), the two points A (0 T) and B (7 T) are critical points for the observation of anisotropic optical conductivity along different crystal directions. From Figure 5a, we see that point A does not depend markedly on temperature when  $T < 200$  K, while it blue shifts with increasing temperature when  $T > 200$  K, whereas point B remains roughly constant over a wide temperature range. This effect can be more vividly observed in Figure 5b, where the relationship between the thermal energy  $k_B T$  and  $\Delta f$  (the frequency difference between

A and B points) is plotted. We find that  $\Delta f$  remains nearly a constant of  $\sim 0.05$  THz up to 17.2 meV (or 200 K) and then sharply shifts to larger values when  $k_B T > 17.2$  meV.

It is known that the inverse triangular spin structure of magnetic octupoles breaks the macroscopic time-reversal symmetry, which leads to a novel Weyl antiferromagnetic state of  $\text{Mn}_3\text{Sn}$  at room temperature. Below a temperature  $T_M$  ( $\sim 260$ – $280$  K),  $\text{Mn}_3\text{Sn}$  enters into the helical state in which the anomalous Hall effect can be quenched [30–32]. This is due to the break in the translational symmetry along the  $c$ -axis in  $\text{Mn}_{3+0.53}\text{Sn}$  films. At a lower critical temperature  $T_1$  ( $\sim 180$ – $200$  K), the nature of spin glass state with a weak ferromagnetism (spin canting towards the  $c$ -axis) is also exhibited [2,33,34]. The results shown in Figure 5a and 5b suggest that an onset of transition may start from  $\sim 200$  K, which corresponds to a transition temperature of  $T_1$  rather than  $T_M$ . A similar effect has been reported very recently via the observation of the THz anomalous Hall effect [2]. In nanostructured  $\text{Mn}_3\text{Sn}$  films, the intrinsic thermal evolution of spin texture inevitably encounters a disordered surface spin structure. It is allowable since the surface spin structure exists in the higher energy state, deviated from the perfect ground state, which blocks the appearance of pure magnetic octupoles in nanostructured  $\text{Mn}_3\text{Sn}$ . The mechanism of field cooling can establish a magnetic-field-induced surface spin texture (ferromagnetic), which exerts an influence on the spin texture in the kagome plane through the weak magnetization. Hence, the anisotropic behaviors in the optoelectronic properties become more distinct at room temperature due to the enhancement of the polarization of magnetic octupoles.

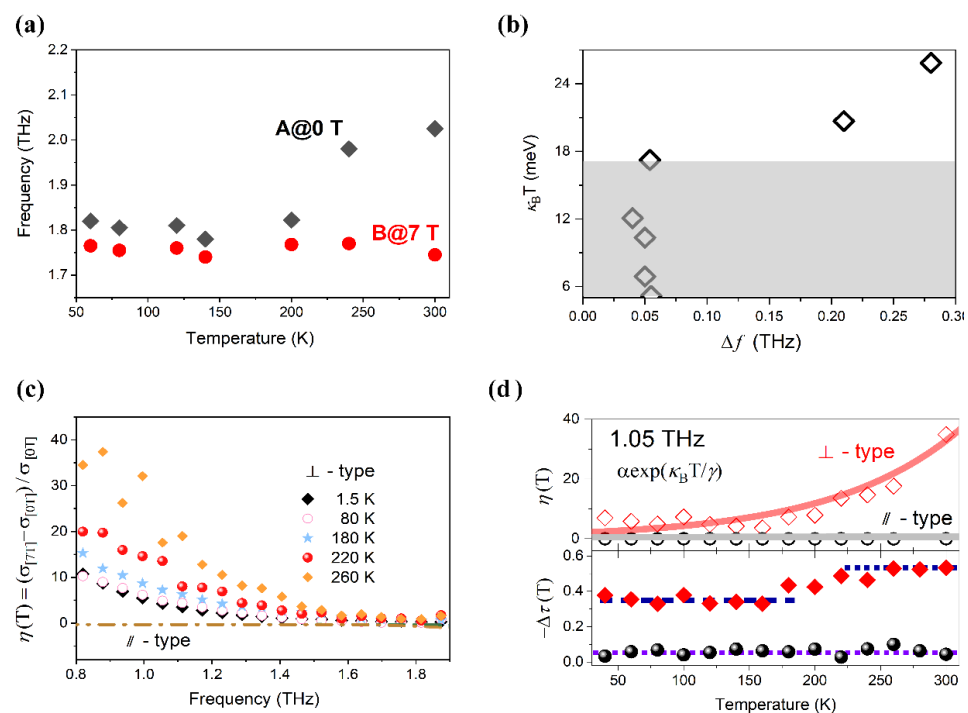


**Figure 5.** The analysis of THz measurements of 40 nm  $\text{Mn}_{3+0.53}\text{Sn}$  samples. (a) The temperature dependence of the intersected points A and B. (b) The relationship between  $k_B T$  and  $\Delta f$  (the frequency difference between A and B points). (c) The ratio  $\eta(T) = [\text{Re}\sigma(7 \text{ T}) - \text{Re}\sigma(0 \text{ T})] / \text{Re}\sigma(0 \text{ T})$  in 0.8–1.9 THz range at different temperatures for // - and  $\perp$  - type samples. (d) Top:  $\eta(T)$  at 1.05 THz for // - and  $\perp$  - type samples. The result from an empirical formula,  $\eta(T) = \alpha \exp(k_B T / \gamma)$ , is drawn for fitting to the experimental data, where  $\alpha$  and  $\gamma$  are fitting parameters; bottom: the temperature dependence of magnetic-field-induced THz transmittance difference  $-\Delta\tau$  at 1.05 THz for // - and  $\perp$  - type samples. Here,  $\Delta\tau = \tau[7 \text{ T}] - \tau[0 \text{ T}]$ .

Finally, in Figure 5c we show the ratio  $\eta(T) = [\text{Re}\sigma(7 \text{ T}) - \text{Re}\sigma(0 \text{ T})] / \text{Re}\sigma(0 \text{ T})$  in the 0.8–1.9 THz range at different temperatures for both // - and  $\perp$  - type samples to evaluate the

effect of the presence of the magnetic field.  $\eta(T)$  for // -type samples shows a surprisingly weak dependence on frequency or temperature. In sharp contrast, in the case of the  $\perp$  -type samples,  $\eta(T)$  decreases monotonically with increasing  $f$  in the frequency range of 0.8–1.9 THz and converges at  $\sim 1.6$  THz, with a relatively small variation at the high THz bandwidth (1.6–1.9 THz). The two sets of data,  $\eta(1.5$  K) and  $\eta(80$  K), almost overlap, while there is a remarkable difference between  $\eta(220$  K) and  $\eta(260$  K). The main feature of the temperature dependence of  $\eta(T)$  is emphasized in Figure 5d (Top). In a wide temperature range,  $\eta(T)$  for // -type film remains roughly the same, while  $\eta(T)$  has an abrupt increase starting from  $\sim 180$ – $200$  K and  $\eta(300$  K) reaches 35 (corresponding to a 35 times change in THz conductivity) for  $\perp$  -type samples. The experimental data can be fitted nicely by a simple empirical formula:  $\eta(T) = \alpha e^{k_B T / \gamma}$ , with  $\alpha$  and  $\gamma$  being the fitting parameters. The value of dimensionless quantity  $\alpha$  in the two cases is similar, which reflects that the difference between // - and  $\perp$  -type samples is relatively small at low temperature. However, the physical quantity  $\gamma$  with a dimension of energy differs by one order of magnitude for // - and  $\perp$  -type samples. The former one is  $\sim 100$  meV and the latter one is less than 10 meV, implying the existence of a huge difference in the thermal spin excitation in the kagome physics of  $\text{Mn}_3\text{Sn}$ . Furthermore, as shown in Figure 5d (Bottom), the  $-\Delta\tau$  of // -type samples has a weak dependence upon temperature. In contrast, the absolute value of  $\Delta\tau$  reaches 0.6 at room temperature in  $\perp$  -type samples, which manifests the recovery of the spin texture of the kagome plane in nanostructured  $\text{Mn}_3\text{Sn}$  films.

#### 4. Conclusions

In this study, we demonstrated firstly that OR can be applied to acquire either // - or  $\perp$  -type nanostructured  $\text{Mn}_3\text{Sn}$  samples on (0001)  $c$ - $\text{Al}_2\text{O}_3$ . It not only enabled us to investigate the fascinating kagome physics of  $\text{Mn}_3\text{Sn}$ , but also sheds light on a method for the fabrication of nanodevices. Most significantly, a huge magnetic-field-induced difference in THz transmittance in  $\perp$  -type thin films was confirmed experimentally in a wide temperature range. The distinct anisotropic THz properties of the samples with different spin textures were also confirmed. Moreover, these phenomena involve the exquisite magnetic dynamics of kagome physics under the influence of surficial spin structures, which embraces an entirely new territory for topological manipulation through the marriage between surface spin structures and topological states. The important and interesting findings from our work demonstrate that topological THz devices based on the elegant kagome physics of  $\text{Mn}_3\text{Sn}$  are worthy of exploration.

**Supplementary Materials:** The following supporting information can be downloaded at: <https://www.mdpi.com/article/10.3390/coatings12081201/s1>, Figure S1: Cross-sectional SEM images of  $\text{Mn}_{3+0.53}\text{Sn}$  films. From top to bottom, the images are corresponding to S4 (40 nm), S6 (120 nm) and S1 (240 nm), respectively; Figure S2: Structural characterization of 60 nm  $\text{Mn}_{3+0.53}\text{Sn}$  films deposited at different substrate temperature. From the top to the bottom, they are S7, S8, S9 and S10; Figure S3: Structural evolution of // -type  $\text{Mn}_{3+0.53}\text{Sn}$  films with different thickness. SEM images of  $\text{Mn}_{3+0.53}\text{Sn}$  films, (a) S11 (40 nm), (b) S7 (60 nm), (c) S12 (120 nm), (d) S13 (180 nm), (e) S14 (240 nm) and (f) S15 (300 nm). (g) XRD pattern of the samples in (a–f). The insert one is the details around the (0002) peak of  $\text{Mn}_3\text{Sn}$  ( $39.20^\circ$ – $40.45^\circ$ ), from which a distortion peak (D peak) can be observed at the right side of (0002) peak while the thickness is larger than 120 nm. (h) The position of the two peaks versus film thickness. The dash line for standard value of  $\text{Mn}_3\text{Sn}$  (0002) is also drawn together.; Table S1: List of samples on (0001)  $c$ - $\text{Al}_2\text{O}_3$  without seed layer.

**Author Contributions:** Conceptualization, S.Y., X.W. and H.W.; Methodology, S.Y., X.W. and H.W.; Investigation, X.W., S.Y., Q.W. (Qiuji Wang), Q.W. (Qian Wang), T.X. and J.G.; Resources, W.X., Y.S., Y.L., J.W. and H.W.; Data Curation, X.W., Q.W. (Qiuji Wang), T.X., Q.W. (Qian Wang) and J.G.; Writing—Original Draft Preparation, S.Y., X.W. and H.W.; Writing—Review and Editing, S.Y. and H.W.; Visualization, H.W.; Supervision, H.W.; Project Administration, J.Z. and H.W.; Funding Acquisition, W.X., Y.S., C.Z. and H.W. All authors have read and agreed to the published version of the manuscript.

**Funding:** This research was funded by the Capacity Building for Sci-Tech Innovation- Fundamental Scientific Research Funds (20530290006 and 20530290044). This work was also supported by the National Key Project of Research and Development (No. 2021YFB3200102), the National Natural Science Foundation of China (62071312, U1930116, U206720039), and by the BRICS STI Framework Programme through NSFC (No. 51861145309).

**Institutional Review Board Statement:** No applicable.

**Informed Consent Statement:** No applicable.

**Data Availability Statement:** The data presented in this study are available on request from the corresponding author (Hai Wang).

**Acknowledgments:** Thanks to the Lab for Multifunctional Ultrafast Magneto-Optical Measurements and the School of Physics and Astronomy, Yunnan University, for the help on the THz measurements.

**Conflicts of Interest:** The authors declare no conflict of interest.

## References

1. Kuroda, K.; Tomita, T.; Suzuki, M.T.; Bareille, C.; Nugroho, A.A.; Goswami, P.; Ochi, M.; Ikhlas, M.; Nakayama, M.; Akebi, S.; et al. Evidence for magnetic Weyl fermions in a correlated metal. *Nat. Mater.* **2017**, *16*, 1090–1095. [[CrossRef](#)] [[PubMed](#)]
2. Matsuda, T.; Kanda, N.; Higo, T.; Armitage, N.P.; Nakatsuji, S.; Matsunaga, R. Room-temperature terahertz anomalous Hall effect in Weyl antiferromagnet Mn<sub>3</sub>Sn thin films. *Nat. Commun.* **2020**, *11*, 909. [[CrossRef](#)] [[PubMed](#)]
3. Khadka, D.; Thapaliya, T.R.; Parra, S.H.; Han, X.Y.; Wen, J.J.; Need, R.F.; Khanal, P.; Wang, W.G.; Zang, J.D.; Kikkawa, M.J.; et al. Kondo physics in antiferromagnetic Weyl semimetal Mn<sub>3+x</sub>Sn<sub>1-x</sub> films. *Sci. Adv.* **2020**, *6*, eabc19776. [[CrossRef](#)] [[PubMed](#)]
4. Nakatsuji, S.; Kiyohara, N.; Higo, T. Large anomalous Hall effect in a non-collinear antiferromagnet at room temperature. *Nature* **2015**, *527*, 212–215. [[CrossRef](#)]
5. Takeuchi, Y.; Yamane, Y.; Yoon, J.; Itoh, R.; Jinnai, B.; Kanai, S.; Ieda, J.; Fukami, S.; Ohno, H. Chiral-spin rotation of non-collinear antiferromagnet by spin-orbit torque. *Nat. Mater.* **2021**, *20*, 1364–1370. [[CrossRef](#)]
6. Tsai, H.; Higo, T.; Kondou, K.; Nomoto, T.; Sakai, A.; Kobayashi, A.; Nakano, T.; Yakushiji, K.; Arita, R.; Miwa, S.; et al. Electrical manipulation of a topological antiferromagnetic state. *Nature* **2020**, *580*, 608–612. [[CrossRef](#)]
7. Higo, T.; Man, H.Y.; Gopman, D.B.; Wu, L.; Koretsune, T.; van't Erve, O.M.J.; Kabanov, Y.P.; Rees, D.; Li, Y.F.; Suzuki, M.T.; et al. Large magneto-optical Kerr effect and imaging of magnetic octupole domains in an antiferromagnetic metal. *Nat. Photonics* **2018**, *12*, 73–78. [[CrossRef](#)]
8. Markou, A.; Taylor, J.M.; Kalache, A.; Werner, P.; Parkin, S.S.P.; Felser, C. Noncollinear antiferromagnetic Mn<sub>3</sub>Sn films. *Phys. Rev. Mater.* **2018**, *2*, 051001. [[CrossRef](#)]
9. Ikeda, T.; Tsunoda, M.; Oogane, M.; Oh, S.J.; Morita, T.; Ando, Y. Fabrication and evaluation of highly c-plane oriented Mn<sub>3</sub>Sn thin films. *AIP Adv.* **2020**, *10*, 015310. [[CrossRef](#)]
10. You, Y.F.; Chen, X.Z.; Zhou, X.F.; Gu, Y.D.; Zhang, R.Q.; Pan, F.; Song, C. Anomalous Hall effect-like behavior with in-plane magnetic field in noncollinear antiferromagnetic Mn<sub>3</sub>Sn films. *Adv. Electron. Mater.* **2019**, *5*, 1800818. [[CrossRef](#)]
11. Kondou, K.; Chen, H.; Tomita, T.; Ikhlas, M.; Higo, T.; MacDonald, A.H.; Nakatsuji, S.; Otani, Y.C. Giant field-like torque by the out-of-plane magnetic spin Hall effect in a topological antiferromagnet. *Nat. Commun.* **2021**, *12*, 6491. [[CrossRef](#)]
12. Li, X.K.; Collignon, C.; Xu, L.C.; Zuo, H.K.; Cavanna, A.; Gennser, U.; Mailly, D.; Fauqué, B.; Balents, L.; Zhu, Z.W.; et al. Chiral domain walls of Mn<sub>3</sub>Sn and their memory. *Nat. Commun.* **2019**, *10*, 3021. [[CrossRef](#)]
13. Kimata, M.; Chen, H.; Kondou, K.; Sugimoto, S.; Muduli, P.K.; Ikhlas, M.; Omori, Y.; Tomita, T.; MacDonald, A.H.; Nakatsuji, S.; et al. Magnetic and magnetic inverse spin Hall effects in a non-collinear antiferromagnet. *Nature* **2019**, *565*, 627–630. [[CrossRef](#)]
14. Ikhlas, M.; Tomita, T.; Koretsune, T.; Suzuki, M.T.; Hamane, D.N.; Arita, R.; Otani, Y.; Nakatsuji, S. Large anomalous Nernst effect at room temperature in a chiral antiferromagnet. *Nat. Phys.* **2017**, *13*, 1085–1090. [[CrossRef](#)]
15. Ikeda, T.; Tsunoda, M.; Oogane, M.; Oh, S.J.; Morita, T.; Ando, Y. Anomalous Hall effect in polycrystalline Mn<sub>3</sub>Sn thin films. *Appl. Phys. Lett.* **2018**, *113*, 222405. [[CrossRef](#)]
16. Higo, T.; Qu, D.R.; Li, Y.F.; Chien, C.L.; Otani, Y.; Nakatsuji, S. Anomalous Hall effect in thin films of the Weyl antiferromagnet Mn<sub>3</sub>Sn. *Appl. Phys. Lett.* **2018**, *113*, 202402. [[CrossRef](#)]
17. Chen, T.S.; Tomita, T.; Minami, S.; Fu, M.X.; Koretsune, T.; Kitatani, M.; Muhammad, I.; Hamane, D.N.; Ishii, R.; Ishii, F.; et al. Anomalous transport due to Weyl fermions in the chiral antiferromagnets Mn<sub>3</sub>X, X = Sn, Ge. *Nat. Commun.* **2021**, *12*, 572. [[CrossRef](#)]
18. Suzuki, M.T.; Koretsune, T.; Ochi, M.; Arita, R. Cluster multipole theory for anomalous Hall effect in antiferromagnets. *Phys. Rev. B* **2017**, *95*, 094405. [[CrossRef](#)]
19. Wan, X.G.; Turner, A.M.; Vishwanath, A.; Savrasov, S.Y. Topological semimetal and Fermi-arc surface states in the electronic structure of pyrochlore iridates. *Phys. Rev. B* **2011**, *83*, 205101. [[CrossRef](#)]
20. Kren, E.; Paitz, J.; Zimmer, G.; Zsoldos, E. Study of the magnetic phase transformation in the Mn<sub>3</sub>Sn phase. *Phys. B* **1975**, *80*, 226–230. [[CrossRef](#)]

21. Yoon, J.Y.; Takeuchi, Y.; DuttaGupta, S.; Yamane, Y.; Kanai, S.; Ieda, J.; Ohno, H.; Fukami, S. Correlation of anomalous Hall effect with structural parameters and magnetic ordering in  $Mn_{3+x}Sn_{1-x}$  thin films. *AIP Adv.* **2021**, *11*, 065318. [[CrossRef](#)]
22. Lozovoy, K. Comparative analysis of germanium-silicon quantum dots formation on Si(100), Si(111) and Sn/Si(100) surfaces. *Nanotechnology* **2018**, *29*, 054002.
23. Bartelt, N.C. Ostwald ripening of two-dimensional islands on Si(001). *Phys. Rev. B* **1995**, *54*, 11741–11751. [[CrossRef](#)]
24. Lifshitz, I.M.; Slyozov, V.V. The kinetics of precipitation from supersaturated solid solutions. *J. Phys. Chem. Solids* **1961**, *19*, 35–50. [[CrossRef](#)]
25. Wagner, C. Theorie der alterung von niederschlagen durch umlosen (Ostwald-Reifung). *Z. Elektrochem.* **1961**, *65*, 581–591. [[CrossRef](#)]
26. Di Vece, M.; Bals, S.; Verbeeck, J.; Lievens, P.; Van Tendeloo, G. Compositional Changes of Pd-Au Bimetallic Nanoclusters upon Hydrogenation. *Phys. Rev. B* **2009**, *80*, 125420. [[CrossRef](#)]
27. Alloyeau, D.; Prevot, G.; Le Bouar, Y.; Oikawa, T.; Langlois, C.; Loiseau, A.; Ricolleau, C. Ostwald Ripening in Nanoalloys: When thermodynamics drives a size-dependent particle composition. *Phys. Rev. Lett.* **2010**, *105*, 255901. [[CrossRef](#)]
28. Prevot, G.; Nguyen, N.T.; Alloyeau, D.; Ricolleau, C.; Nelayah, J. Ostwald-Driven Phase Separation in Bimetallic Nanoparticle Assemblies. *ACS Nano* **2016**, *10*, 4127–4133. [[CrossRef](#)]
29. Tumbul, A.; Gökteş, A.; Zarbali, M.Z.; Aslan, F. Structural, morphological and optical properties of the vacuum-free processed CZTS thin film absorbers. *Mater. Res. Express* **2018**, *5*, 066408. [[CrossRef](#)]
30. Cable, J.W.; Wakabayashi, N.; Radhakrishna, P. A neutron study of the magnetic-structure of  $Mn_3Sn$ . *Solid State Commun.* **1993**, *88*, 161–166. [[CrossRef](#)]
31. Ohmori, H.; Tomiyoshi, S.; Yamauchi, H.; Yamamoto, H. Spin structure and weak ferromagnetism of  $Mn_3Sn$ . *J. Magn. Magn. Mater.* **1987**, *70*, 249–251. [[CrossRef](#)]
32. Sung, N.H.; Ronning, F.; Thompson, J.D.; Bauer, E.D. Magnetic phase dependence of the anomalous Hall effect in  $Mn_3Sn$  single crystals. *Appl. Phys. Lett.* **2018**, *112*, 132406. [[CrossRef](#)]
33. Cheng, B.; Wang, Y.C.; Barbalas, D.; Higo, T.; Nakatsuji, S.; Armitage, N.P. Terahertz conductivity of the magnetic Weyl semimetal  $Mn_3Sn$  films. *Appl. Phys. Lett.* **2019**, *115*, 012405. [[CrossRef](#)]
34. Tomiyoshi, S.; Abe, S.; Yamaguchi, Y.; Yamauchi, H.; Yamamoto, H. Triangular spin structure and weak ferromagnetism of  $Mn_3Sn$  at low temperature. *J. Magn. Magn. Mater.* **1986**, *54–57*, 1001–1002. [[CrossRef](#)]